npj | Computational Materials

www.nature.com/npjcompumats

ARTICLE OPEN

Dynamics of antipolar distortions

Kinnary Patel[1], Sergey Prosandeev[1,2] and Laurent Bellaiche[1]

Materials possessing antipolar cation motions are currently receiving a lot of attention because they are fundamentally intriguing while being technologically promising. Most studies devoted to these complex materials have focused on their static properties or on their zone-center phonons. As a result, some important dynamics of antipolar cation distortions, such as the temperature behavior of their phonon frequencies, have been much less investigated, despite the possibility to exhibit unusual features. Here, we report the results and analysis of atomistic simulations revealing and explaining such dynamics for $BiFeO_3$ bulks being subject to hydrostatic pressure. It is first predicted that cooling such material yields the following phase transition sequence: the cubic paraelectric $Pm\bar{3}m$ state at high temperature, followed by an intermediate phase possessing long-range-ordered in-phase oxygen octahedral tiltings, and then the Pnma state that is known to possess antipolar cation motions in addition to in-phase and antiphase oxygen octahedral tiltings. Antipolar cation modes are found to all have high phonon frequencies that are independent of temperature in the paraelectric phase. On the other hand and in addition to antipolar cation modes increasing in number, some phonons possessing antipolar cation character are rather soft in the intermediate and Pnma states. Analysis of our data combined with the development of a simple model reveals that such features originate from a dynamical mixing between pure antipolar cation phonons and fluctuations of oxygen octahedral tiltings, as a result of a specific trilinear energetic coupling. The developed model can also be easily applied to predict dynamics of antipolar cation motions for other possible structural paths bringing $Pm\bar{3}m$ to Pnma states.

npj Computational Materials (2017)3:34 ; doi:10.1038/s41524-017-0033-z

INTRODUCTION

Trilinear energetic couplings have been recently discovered and intensively investigated in oxides, as mostly motivated by the fact that they can result in the formation of an electrical polarization because of its coupling with two other physical quantities. Examples of these two latter quantities are two different oxygen octahedral tiltings,[1–7] one oxygen octahedral tiling and one antipolar motion,[8] one Jahn-Teller mode and one antiferrodistortive (or antipolar) distortion,[9, 10] or even two pseudo-Jahn-Teller motions.[11] Note also that trilinear energetic couplings do not restrain themselves to polar materials since they can also arise in compounds possessing antipolar cation distortions via their couplings with antiphase and inphase octahedral tiltings.[12] Antipolar systems are important compounds on their own. For instance, the Pnma state in ABO_3 perovskites is known to possess antipolar motions of its A cations and recent studies found that it can also adopt the double polarization-vs.-electric field hysteresis loop in some materials[13, 14] that is characteristics of antiferroelectrics[15]—therefore suggesting that Pnma states in some perovskites can hold promise towards the design of energy storage devices with high energy densities and efficiencies.[16–22]

Interestingly, all the aforementioned works on trilinear energetic couplings have been aimed at revealing and understanding resulting *static* properties. In other words, the effect of these original trilinear couplings on *dynamics* have been left out so far and are thus basically unknown, to the best of our knowledge. For instance, one may wonder how antipolar phonons behave with temperature when the material exhibits phase transitions leading to an antipolar state having also antiphase and in-phase oxygen octahedral tiltings (as the Pnma state, which is the most common structural phase adopted by perovskites,[23, 24] does). For instance, can they be soft in any phase, including the one(s) for which the antipolar cation motions have not adopted yet a long-range order? Can they mix with phonons associated with fluctuations of oxygen octahedral tiltings in any of these phases because of this trilinear energetic coupling, or rather does this hypothetical mixing only occurs when in-phase and/or antiphase tiltings have condensed?

The aim of this manuscript is to provide answers to all these questions by focusing on a specific material, namely $BiFeO_3$ (BFO) under hydrostatic pressure, because it is known to adopt the Pnma state at high enough pressure[25–27] and because we are in possession of an atomistic approach that allows us to mimic its dynamical properties at finite temperature.

RESULTS

We employ the effective Hamiltonian[28] approach to perform first Monte-Carlo (MC) simulations and to compute finite-temperature properties of BFO bulk under a simulated hydrostatic pressure of about 17.2 GPa in $12 \times 12 \times 12$ supercells using 40,000 MC sweeps. The comparison between experimental measurements[25] and similar computations showed that this simulated pressure likely corresponds to an experimental pressure of about 8.2 GPa, probably because of the typical underestimation of the lattice constant by first-principles techniques and to correct for the fact that the parameters of the effective Hamiltonian of BFO were all

[1]Physics Department and Institute for Nanoscience and Engineering, University of Arkansas, Fayetteville, AR 72701, USA and [2]Institute of Physics and Physics Department of Southern Federal University, Rostov-na-Donu 344090, Russia
Correspondence: Kinnary Patel (kypatel@email.uark.edu)

Received: 20 January 2017 Revised: 27 June 2017 Accepted: 7 July 2017
Published online: 21 August 2017

determined from *ab-initio* calculations at atmospheric pressure. Note that BFO is known to acquire a Pnma space group at high enough temperature at atmospheric pressure[28, 29] while it is R3c at lower temperatures[30] or even to be the ground state of BFO under high-enough pressure (see refs. 25–27 and references therein).

We also performed here Molecular Dynamics (MD) calculations in the frame of the same effective Hamiltonian method (see the Methods Section and Supplemental Materials), and we used the results of these calculations to compute frequency-dependent responses related to different order parameters, as described by using the following general formula[31–33]

$$\chi^{AA}_{\alpha\beta}(\nu) = \langle A_\alpha(t)A_\beta(t)\rangle + i2\pi\nu \int_0^\infty dt\, e^{i2\pi\nu t}\langle A_\alpha(t)A_\beta(0)\rangle \quad (1)$$

where ν is the frequency, while α and β define Cartesian components. $A(t)$ is an order parameter at time t, and "$\langle..\rangle$" indicates thermal average.

For instance and since we are interested in antipolar phonons, A will be chosen to be the $\boldsymbol{u}_X$ vector characterizing the X_5^+ antipolar Bi displacements at the X-point of the Brillouin zone, and that is given by $\boldsymbol{u}_X = \frac{1}{N}\sum_i \boldsymbol{u}_i(-1)^{n_z(i)}$, where N is the number of the Bi ions in the supercell, and $n_z(i)$ is an integer locating the cell i along the z-axis[34]; here $\boldsymbol{u}_i$ is the local mode in unit cell i, which is centered on a Bi site (see Method Section). As we will see below, it is also worthwhile to investigate $\chi^{AA}_{\alpha\beta}(\nu)$ for which A are the following two vectors: (i) The antiphase oxygen octahedral tilting R_4^+ mode, $\boldsymbol{\omega}_R = \frac{1}{N}\sum_i \boldsymbol{\omega}_i(-1)^{n_x(i)+n_y(i)+n_z(i)}$, where[34] $n_x(i)$, $n_y(i)$, and $n_z(i)$ are integers locating the cell i in x, y, and z directions, respectively; here $\boldsymbol{\omega}_i$ is an Fe-centered pseudo-vector that characterizes the oxygen octahedral tilting in unit cell i (see Method Section); and (ii) The in-phase oxygen octahedral tilting around the Fe sites associated with the M_3^+ mode, $\boldsymbol{\omega}_M = \frac{1}{N}\sum_i \boldsymbol{\omega}_i(-1)^{n_x(i)+n_y(i)}$. Note that these three quantities are coupled via a trilinear energy, which can be inferred from the seventh atomistic term of Eq. (9) indicated in the Method Section, and that can take the following form[12]:

$$E_{trilinear} = D\left(u_{X,x}\omega_{R,x}\omega_{M,z} + u_{X,y}\omega_{R,y}\omega_{M,z}\right) \quad (2)$$

where D is a coefficient characterizing the strength of the interaction and where the second subscript indicated in the involved physical quantities refers to the corresponding Cartesian component of $\boldsymbol{u}_X$, $\boldsymbol{\omega}_R$ and $\boldsymbol{\omega}_M$. In the continuous approximation, this trilinear energetic coupling of Eq. (2) can be expressed as $E_{trilinear} = D\ [\boldsymbol{u}\cdot\nabla\times(\boldsymbol{\omega}_R\times\boldsymbol{\omega}_M) + (\boldsymbol{\omega}_R\times\boldsymbol{\omega}_M)\cdot\nabla\times\boldsymbol{u}]$, which can be used to develop novel phenomenologies incorporating trilinear couplings. In this equality, $\nabla\times(\boldsymbol{\omega}_R\times\boldsymbol{\omega}_M)$ is the (Bi-sites-centered) curl of the cross-product of the R- and M-tilting modes' pseudo vectors and $\nabla\times\boldsymbol{u}$ is the (Fe-sites-centered) curl of the local mode. These two curls can be computed from atomistic simulations via finite differences by considering the eight Fe sites nearest to the Bi-site center of the local mode and the eight Bi sites nearest to the Fe-site center of the tilting modes, respectively. (note also that this trilinear energy coupling is finite in, e.g., the Pnma state while it vanishes in, e.g., the R3c phase).

Interestingly, $\chi^{AA}_{\alpha\beta}(\nu)$ can be considered to be a complex "susceptibility" related to A, that is it represents the response of A to its conjugate field. Such "susceptibility" is not measurable (unlike the dielectric susceptibility) when A is chosen to be $\boldsymbol{u}_X$, $\boldsymbol{\omega}_R$ or $\boldsymbol{\omega}_M$ (because their conjugate fields are staggered fields). However, the peaks of the imaginary part of the susceptibilities associated with $\boldsymbol{u}_X$, $\boldsymbol{\omega}_R$ and $\boldsymbol{\omega}_M$, respectively, occur at the natural frequencies of phonons associated with antipolar motions, antiphase tiltings, and in-phase tiltings, respectively. It is precisely the determination of these natural frequencies we are interested in, which explains why we decided to compute these $\chi^{AA}_{\alpha\beta}(\nu)$ responses and which also explains why we do not incorporate the factor[31–33] $\frac{1}{\varepsilon_0 V k_B T}$ into Eq. (1), because it is not important in our problem, where V is the volume of the chosen supercell, k_B is the Boltzmann constant and ε_0 defines the vacuum permittivity. Note that these phonon frequencies may be experimentally obtained by hyper Raman scattering techniques.[35]

Moreover, for any investigated temperature, we typically fit the three different aforementioned types of computed $\chi^{AA}_{\alpha\beta}(\nu)$ susceptibilities (associated with the dynamics of the X_5^+, R_4^+ and M_3^+ modes) by a *sum* of Damped Harmonic Oscillators (DHO), given by the formula

$$\chi = \frac{S^2}{\nu_r^2 - \nu^2 - i\nu\gamma} \quad (3)$$

where ν_r, γ, and S are the resonant frequency, damping constant, and oscillator strength, correspondingly. Note that the number of DHOs involved in this summation precisely corresponds to the number of the peaks found in the MD simulations of $\chi^{AA}_{\alpha\beta}(\nu)$.

Let us first report and discuss the temperature dependency of $\boldsymbol{u}_X$, $\boldsymbol{\omega}_R$ or $\boldsymbol{\omega}_M$, as shown in Fig. 1, when cooling BFO under hydrostatic pressure from 1600 to 900 K by steps of 20 K. One can see that these three vectors are all vanishing above 1280 K, which is representative of the cubic paraelectric Pm$\bar{3}$m phase. On the other hand, the z-component of $\boldsymbol{\omega}_M$ becomes finite and strengthens when the temperature is reduced below 1280 K and down to 1240 K, while $\boldsymbol{u}_X$ and $\boldsymbol{\omega}_R$ remain null in this rather small temperature interval. Such behaviors indicate that our studied BFO system is predicted to adopt the P4/mbm ground state between ≃1280 and ≃1240 K. Further cooling the system results in the x- and y-components of $\boldsymbol{u}_X$ becoming finite, equal to each other and increasing in magnitude when decreasing the temperature below 1240 K, exactly as the x- and y-components Cartesian components of $\boldsymbol{\omega}_R$ also do. Moreover, the z-component of $\boldsymbol{\omega}_M$ continues to be non-null and to get enhanced when the temperature is reduced below 1240 K. Our investigated BFO system therefore now adopts the Pnma ground, for which spontaneous $\boldsymbol{u}_X$, $\boldsymbol{\omega}_R$ or $\boldsymbol{\omega}_M$ exist and lie along the pseudo-cubic [110], [1$\bar{1}$0] and [001] directions respectively, below this latter critical temperature (note that the three lattice vectors of the Pnma state lie along the pseudo-cubic [1$\bar{1}$0], [110] and [001] directions, respectively).

In order to determine how these phase transitions affect the dynamics of antipolar mode, Fig. 2a–c display the imaginary part of $\chi^{AA}_{xx}(\nu)$, $\chi^{AA}_{yy}(\nu)$ and $\chi^{AA}_{zz}(\nu)$ respectively, when $A = \boldsymbol{u}_X$, for a temperature of 1560 K—that is within the Pm$\bar{3}$m state. Figure 3a–c report similar data but for a temperature of 1260 K, that is now for

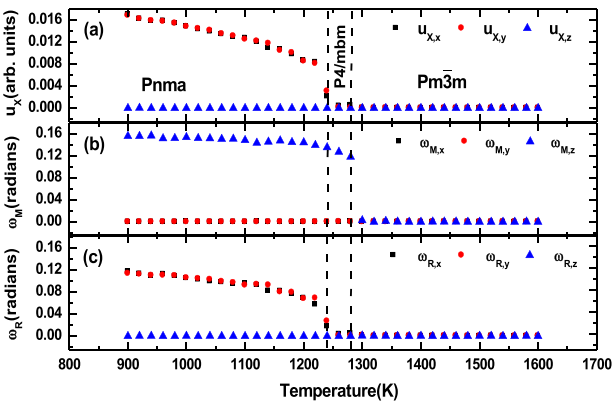

Fig. 1 Predicted temperature dependence of the antipolar $\boldsymbol{u}_X$ vector **a**, in-phase tilting $\boldsymbol{\omega}_M$ pseudo vector **b** and antiphase tilting $\boldsymbol{\omega}_R$ pseudo-vector **c** in our BFO system subject to hydrostatic pressure. The dashed vertical lines delimit three different structural phases (see text)

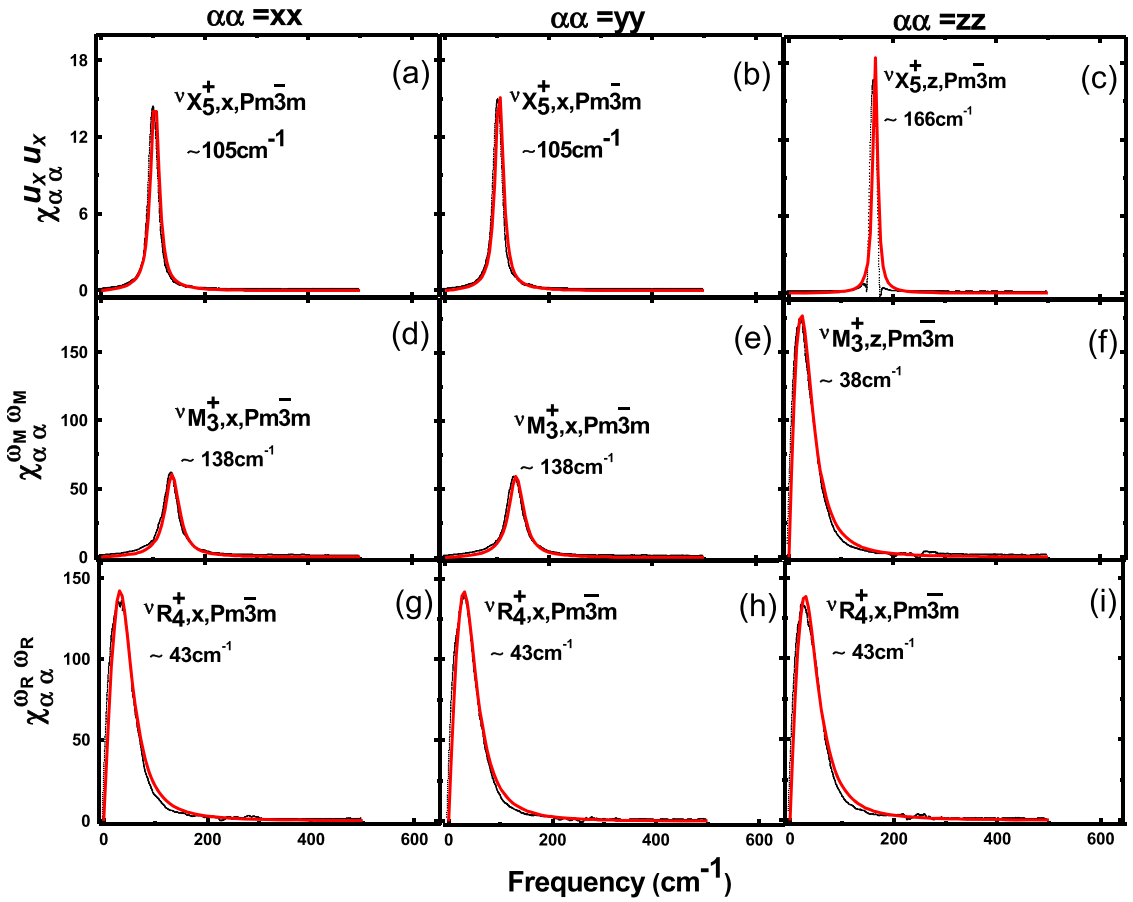

Fig. 2 Frequency dependence of the imaginary part of the $\chi_{\alpha\alpha}^{AA}(\nu)$ "susceptibilities" in our BFO system subject to hydrostatic pressure, for $A = \boldsymbol{u}_X$ **a**–**c**, $\boldsymbol{\omega}_M$ **d**–**f** and $\boldsymbol{\omega}_R$ **g**–**i** at a temperature of 1560 K (that is, for the Pm$\bar{3}$m cubic state). For each physical quantity A, the left, middle and right panels correspond to $\alpha = x$, y or z coordinate, respectively. The black line displays the MD data while the red line represents their fit by DHOs

the P4/mbm phase. Figure 4a–c also show these susceptibilities of the antipolar degree of freedom but at 1040 K, i.e. inside the Pnma state. Different narrow peaks can be clearly seen at 1560 K: one peak occurring at around 105 cm^{-1} in both the *xx* and *yy* components of the susceptibility, which thus corresponds to an antipolar phonon that is doubly degenerate and associated with oscillations of $\boldsymbol{u}_X$ along the *x* or *y* direction. Such frequency will be denoted as $\nu_{X_5^+,x,Pm\bar{3}m}$, adopting the convention that the three subscripts refer to the type of mode, the direction of the fluctuations of its order parameter and the macroscopic phase, respectively. The *zz* component of the susceptibility shown in Fig. 2c has also another peak at a frequency that is close to 166 cm^{-1} and that will be coined $\nu_{X_5^+,z,Pm\bar{3}m}$ (since it is associated with oscillations of $\boldsymbol{u}_X$ along the *z* axis).

Furthermore, Fig. 3a–c reveal that, at 1260 K, the antipolar susceptibility continues to have a *zz* component possessing a single peak, and for which the frequency is now denoted as $\nu_{X_5^+,z,P4/mbm}$ and that is equal to 172 cm^{-1}. On the other hand, its *xx* and *yy* components, while still being very similar to each other, have now two peaks rather than a single one. These two peaks occur at frequencies of about 15 and 120 cm^{-1} at 1260 K and that are coined $\nu_{X_5^+,x,P4/mbm,LF}$ and $\nu_{X_5^+,x,P4/mbm,HF}$ respectively, where "LF" and "HF" stand for low-frequency and high-frequency, respectively.

Interestingly, a further increase of the number of peaks occurs in the *xx* and *yy* components of the antipolar susceptibilities in the Pnma state. As a matter of fact, Fig. 4a, b now show *three* peaks there, that are centered around 80, 115 and 144 cm^{-1} at 1040 K, and that will be denoted as $\nu_{X_5^+,x,Pnma,LF}$, $\nu_{X_5^+,x,Pnma,MF}$ (with "MF" standing for "middle frequency") and $\nu_{X_5^+,x,Pnma,HF}$, respectively. Note that computing the susceptibility of $\boldsymbol{u}_X$ in a different basis indicates (not shown here) that $\nu_{X_5^+,x,Pnma,LF}$ and $\nu_{X_5^+,x,Pnma,MF}$ both mostly correspond to oscillations of antipolar motions along the direction of the spontaneous, long-range-ordered $\boldsymbol{u}_X$ in the Pnma state, while $\nu_{X_5^+,x,Pnma,HF}$ is mostly associated with fluctuations of antipolar motions along the in-plane direction that is perpendicular to this spontaneous $\boldsymbol{u}_X$. On the other hand, the *zz* component of this antipolar susceptibility remains singly peaked at a frequency of about 175 cm^{-1} at 1040 K, to be denoted as $\nu_{X_5^+,z,Pnma}$.

$\nu_{X_5^+,z,Pnma}$, $\nu_{X_5^+,z,P4/mbm}$ and $\nu_{X_5^+,z,Pm\bar{3}m}$ can be considered to be continuation of each other within the phase transition sequence since they are all associated with fluctuations of antipolar motions along the *z*-axis. On the other hand, it is not straightforward to understand the microscopic origin of the increase of the number of peaks occurring in the *xx* and *yy* susceptibilities associated with the X_5^+ mode when passing phase transitions (note that group theory can, of course, predict the increase of the number of phonon modes when changing structural phases, but does not provide the microscopic origin of such increase). For instance, one may wonder what atomistic feature is responsible for the occurrence of two peaks in these susceptibilities in the P4/mbm phase (rather than a single one as in Pm$\bar{3}$m) while the antipolar vector still does not adopt any long-range ordering there. We will come back to this point later on.

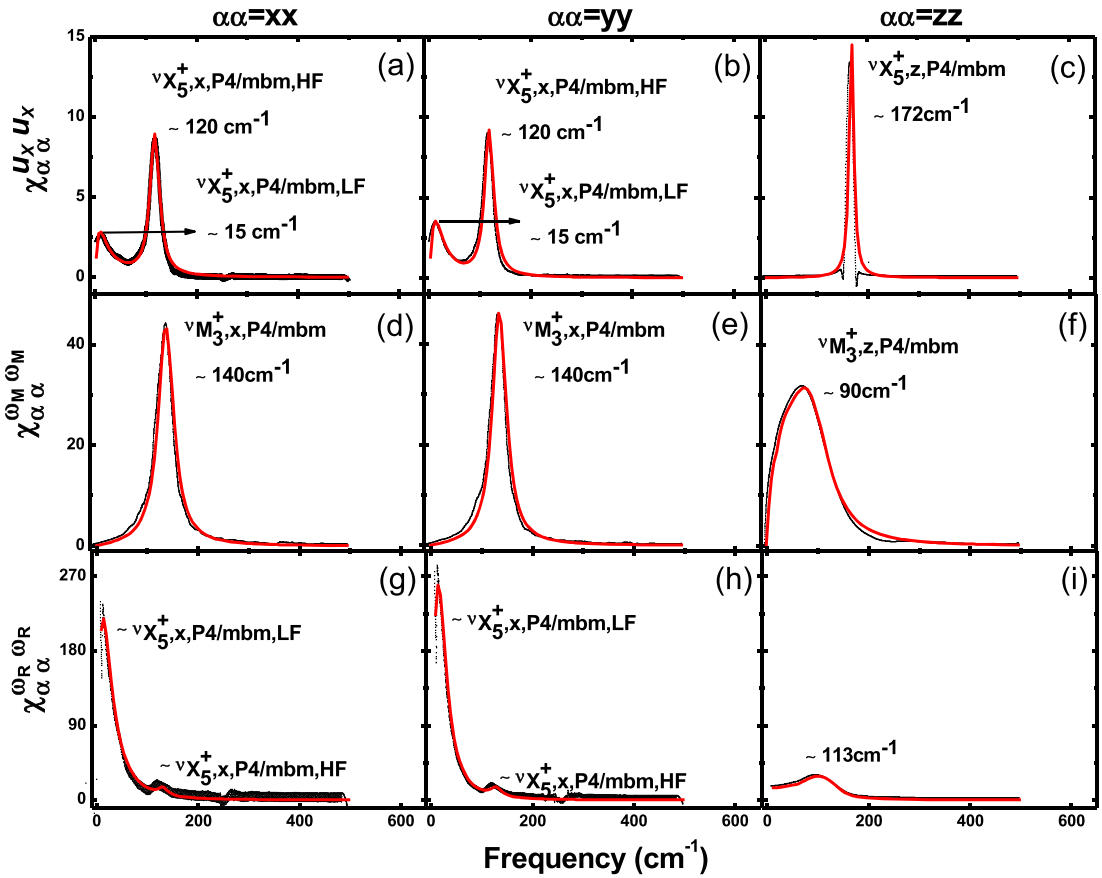

Fig. 3 Same as Fig. 2 but for a temperature of 1260 K (which corresponds to the P4/mbm state)

Meanwhile, let us concentrate on Fig. 5a that shows the temperature dependencies of all aforementioned resonant frequencies associated with the dynamics of Bi motions within the X_5^+ antipolar mode. Several important results can be inferred from this Figure. First of all, both $\nu_{X_5^+,z,Pm\bar{3}m}$ and $\nu_{X_5^+,x,Pm\bar{3}m}$ are nearly independent on temperature within the entire stability region of the cubic state. As a result, neither of these two frequencies softens when approaching the Pm$\bar{3}$m—to—P4m/bm transition from *above*, implying that this transition is dynamically driven by a physical quantity that has nothing to do with antipolar cation motions—as consistent with the sole condensation of the *z*-component of $\boldsymbol{\omega}_M$ below 1280 K (see Fig. 1). On the other hand, one specific antipolar mode, namely $\nu_{X_5^+,x,P4/mbm,LF}$, is very soft within the entire P4/mbm state. Figure 5a also tells us that $\nu_{X_5^+,x,Pnma,LF}$ significantly softens too when heating the system within the Pnma state towards the Pnma-to-P4/mbm transition. In order to understand all these effects, we first decided to turn our attention to the "susceptibilities" of Eq. (3) that are associated with the $\boldsymbol{\omega}_R$ and $\boldsymbol{\omega}_M$ physical quantities.

For that, Fig. 2d–f (respectively, Fig. 2g–i) display the imaginary part of $\chi_{xx}^{AA}(\nu)$, $\chi_{yy}^{AA}(\nu)$ and $\chi_{zz}^{AA}(\nu)$ respectively, when $A = \boldsymbol{\omega}_M$ (respectively, $A = \boldsymbol{\omega}_R$) for a temperature of 1560 K, i.e. within the cubic Pm$\bar{3}$m state. Figures 3d–f and 4d–f (respectively, Figs. 3g–i and 4g–i) provide similar data for the susceptibility associated with the in-phase (respectively, out-of-phase) tiltings at 1260 and 1040 K, respectively, that is for P4/mbm and Pnma states. At 1560 K, the antiphase octahedral tilting R_4^+ mode presents a single peak in either the *xx*, *yy* or *zz* susceptibility with the corresponding natural frequency being identical between the different components of this susceptibility and being coined $\nu_{R_4^+,x,Pm\bar{3}m}$ here. It is about 43 cm^{-1} at 1560 K, is therefore triply degenerate and corresponds to fluctuations of $\boldsymbol{\omega}_R$ along the *x*, *y* or *z* axes. On the other hand, the susceptibilities of the in-phase octahedral tilting M_3^+ mode exhibits two different types of peaks in the cubic state: one at a higher frequency of about 138 cm^{-1} at 1560 K, to be denoted as $\nu_{M_3^+,x,Pm\bar{3}m}$ and that is associated with oscillations of ω_M along the *x* or *y* axes (it is doubly degenerated, as evidenced by the peak occurring at the same frequency in the *xx* and *yy* susceptibilities associated with the in-phase tilting); and a second lowest frequency, $\nu_{M_3^+,z,Pm\bar{3}m}$, close to 38 cm^{-1} at 1560 K and which corresponds to fluctuations of $\boldsymbol{\omega}_M$ along the *z* axis (since it is evidenced in the *zz* component of the susceptibility associated with $\boldsymbol{\omega}_M$). Furthermore, Fig. 5b reports $\nu_{R_4^+,x,Pm\bar{3}m}$ and $\nu_{M_3^+,z,Pm\bar{3}m}$, as a function of temperature in the Pm$\bar{3}$m cubic state. These two frequencies soften when approaching the critical temperature of 1280 K, with $\nu_{M_3^+,z,Pm\bar{3}m}$ being always smaller than $\nu_{R_4^+,x,Pm\bar{3}m}$ for any temperature. Such features are responsible for the occurrence of long-range-ordered *in-phase* tiltings below 1280 K (see Fig. 1), and therefore to the transition from Pm$\bar{3}$m to P4/mbm. It is also interesting to realize that the facts that $\nu_{M_3^+,z,Pm\bar{3}m}$ is different from $\nu_{R_4^+,x,Pm\bar{3}m}$ and that $\boldsymbol{\omega}_M$ condenses at a slightly higher temperature than $\boldsymbol{\omega}_R$ (see Fig. 1) imply that phenomenologies having the same harmonic coefficient in front of in-phase and anti-phase tiltings (see, e.g., ref. 3) have to be revised and generalized as mentioned in the method section.

Let us now pay attention to the peaks of the susceptibilities of the antiphase and in phase tiltings, but now in the P4/mbm state. In particular, comparing Fig. 3g, h with Fig. 2g, h tells us that the *xx* and *yy* susceptibilities associated with $\boldsymbol{\omega}_R$, while still being similar to each other, have now two peaks each, in P4/mbm (unlike in the cubic state), with the corresponding frequencies being close to the aforementioned antipolar frequencies we denoted as $\nu_{X_5^+,x,P4/mbm,LF}$ and $\nu_{X_5^+,x,P4/mbm,HF}$. Such facts strongly hint towards

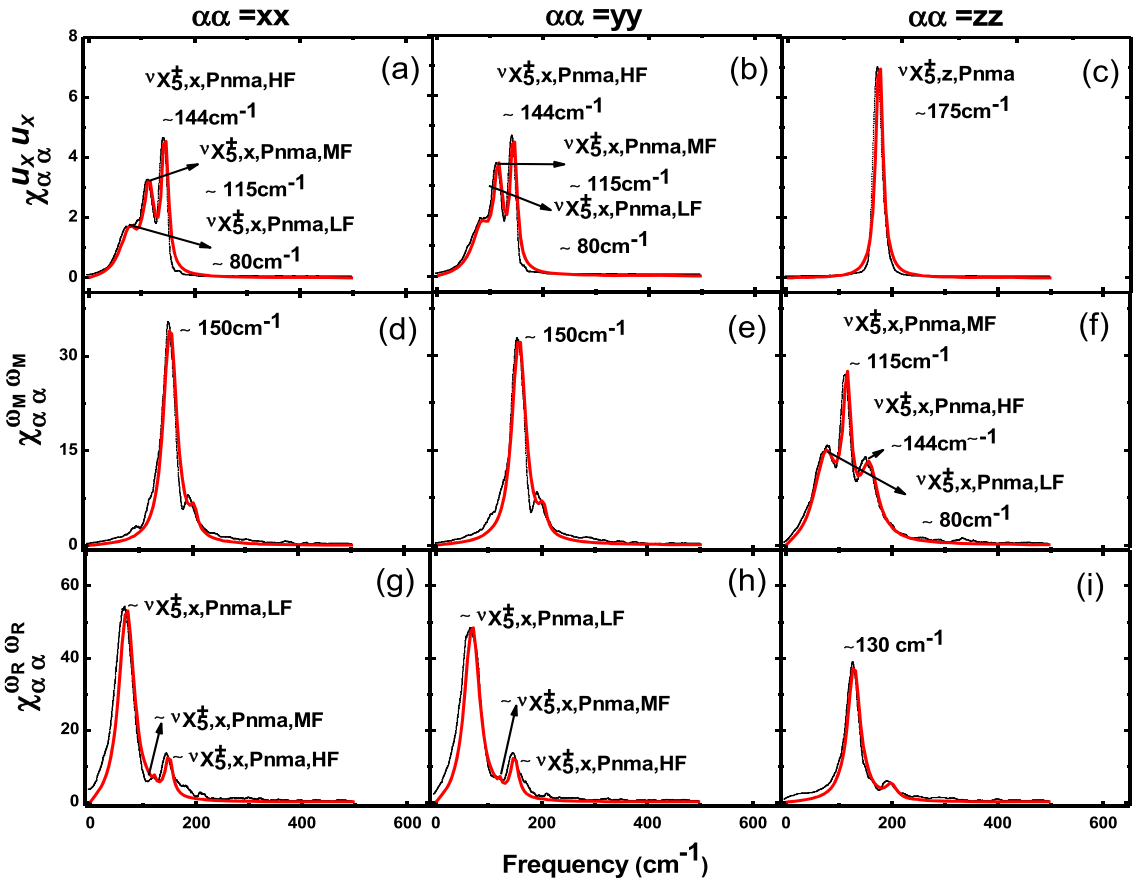

Fig. 4 Same as Fig. 2 but for a temperature of 1040 K (which corresponds to the Pnma state)

a very specific *dynamical* coupling between the fluctuations of the *x*- and *y*-components of $\boldsymbol{u}_X$ and $\boldsymbol{\omega}_R$ within the P4/mbm state. Such hint is reinforced when realizing that $\nu_{X_5^+,x,P4/mbm,LF}$ corresponds to the weakest peak of $\chi^{AA}_{xx}(\nu)$ for $A=\boldsymbol{u}_X$ (see Fig. 3a) while being associated with the strongest peak for the xx-component of the susceptibility of $\boldsymbol{\omega}_R$ (cf Fig. 3g), while the reverse behaviors are seen for $\nu_{X_5^+,x,P4/mbm,HF}$ (i.e., it is now the xx-susceptibility of the antipolar motions rather than of the antiphase tilting that has the strongest peak). This mixing also explains why $\nu_{X_5^+,x-y,Pnma,LF}$ is soft within the P4/mbm state, since the antiphase octahedral tilting is already very soft in the cubic state (see the temperature behavior of $\nu_{R_4^+,x,Pm\bar{3}m}$ in Fig. 5b), and why a phase transition from P4/mbm to Pnma occurs at around 1240 K, below which both the antipolar motions and antiphase tiltings adopt long-range order (in addition to the continuous spontaneous value of the in-phase tilting).

It is also interesting to realize that the *zz*-component of the susceptibility associated with the in-phase-tilting-related $\boldsymbol{\omega}_M$ continues to have a single peak in the intermediate P4/mbm state (to be denoted as $\nu_{M_3^+,z,P4/mbm}$ which is at a much higher frequency that the corresponding $\nu_{M_3^+,z,Pm\bar{3}m}$ of the cubic phase, see Figs. 2f, 3f and 5b) but suddenly exhibits three peaks in the Pnma phase as evidenced in Fig. 4f. Very interestingly, these three peaks have resonant frequencies that are basically identical to the aforementioned antipolar $\nu_{X_5^+,x,Pnma,LF}$, $\nu_{X_5^+,x,Pnma,MF}$ and $\nu_{X_5^+,x,Pnma,HF}$. Moreover, these three resonant frequencies can also be seen within the Pnma state in the *xx* and *yy* susceptibilities of the antiphase-tilting-related $\boldsymbol{\omega}_R$ (see Fig. 4g, h). Such features suggest different mixings of antipolar and AFD modes in the Pnma state, all involving *in-plane* fluctuations of both $\boldsymbol{u}_X$ and $\boldsymbol{\omega}_R$ and *out-of-plane* oscillations of $\boldsymbol{\omega}_M$. This suggestion is also consistent with the magnitude of the peaks, since, e.g., the maximal peaks of $\chi^{AA}_{\alpha\beta}(\nu)$ susceptibilities for $A=\boldsymbol{\omega}_R$, $\boldsymbol{\omega}_M$ and $\boldsymbol{u}_X$ occur at three different frequencies, namely $\nu_{X_5^+,x,Pnma,LF}$ (see Fig. 4g), $\nu_{X_5^+,x,Pnma,MF}$ (see Fig. 4f) and $\nu_{X_5^+,x,Pnma,HF}$ (see Fig. 4a), respectively. This mixing also explains why $\nu_{X_5^+,x,Pnma,LF}$ softens when approaching the Pnma-to-P4/mbm transition since we demonstrated that oxygen octahedral titings are very soft above such transition.

Let us now try to understand why $\boldsymbol{u}_X$ and $\boldsymbol{\omega}_R$ can be dynamically coupled in the P4/mbm state while the fluctuations of $\boldsymbol{u}_X$, $\boldsymbol{\omega}_R$ and $\boldsymbol{\omega}_M$ can all dynamically mix in the Pnma state, and that no such dynamical couplings exists in the cubic phase. Let us also explain why only very specific components of these three order parameters dynamically couple to each other in the P4/mbm and Pnma phases.

DISCUSSION

For that, let us first write the equation of motion associated with the *x* or *y* component of $\boldsymbol{u}_X$:

$$m^X \frac{d^2 u_{X,\alpha}}{dt^2} = -\frac{dE_{total}}{du_{X,\alpha}} + \gamma_\alpha^X \frac{du_{X,\alpha}}{dt} \tag{4}$$

Where $\alpha = x$ or *y*; m^X is the mass of this antipolar mode; γ_α^X is the damping constant; E_{total} is the total energy provided our effective Hamiltonian; and *t* is the time. In the harmonic approximation and using the trilinear energy given by Eq. (2) as well as Equations of the effective Hamiltonian described in the Method Section, Eq. (4) becomes:

$$\sum_\beta \left[\left(2\pi\nu_\alpha^X\right)^2 - (2\pi\nu)^2 - 2i\Gamma_\alpha^X \pi\nu + B_{X_\alpha M_\beta}\omega_{M,\beta}^2 + B_{X_\alpha R_\beta}\omega_{R,\beta}^2 \right] u_{X,\alpha} = -D\omega_{M,z}\omega_{R,\alpha} \tag{5}$$

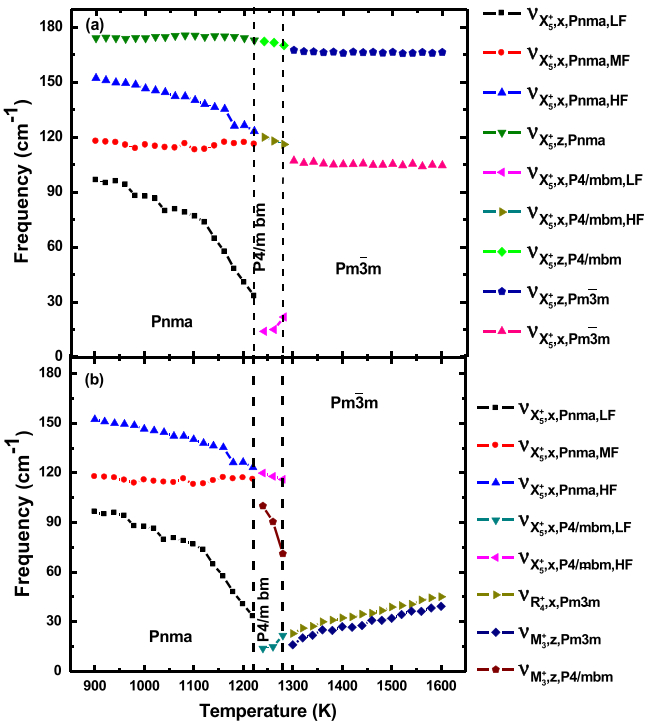

Fig. 5 Temperature dependence of natural frequencies of some phonon modes that have antipolar cation character **a** and/or oxygen octahedral tiltings character **b**. The vertical dashed lines delimit the different phases obtained in the calculations for our BFO system subject to hydrostatic pressure. See text for the notations on this figure

Here ν_a^X is the natural frequency of the antipolar mode, $\Gamma_a^X = \gamma_a^X/m^X$, D is the *trilinear* coupling strength between $\boldsymbol{u}_X$, $\boldsymbol{\omega}_R$ and $\boldsymbol{\omega}_M$, β runs over the Cartesian components, and B are the parameters involved in the biquadratic coupling between u_X^2 and ω_M^2 and between u_X^2 and ω_R^2. D and B here contain a factor of $1/m^X$.

Neglecting fluctuations of $\omega_{M,\beta}$ and $\omega_{R,\beta}$ with time on the left-hand site of Eq. (5) yields

$$\sum_\beta \left[\left(2\pi\nu_a^X\right)^2 - (2\pi\nu)^2 - 2i\Gamma_a^X \pi\nu + B_{X_a M_\beta} \left\langle \omega_{M,\beta}^2 \right\rangle + B_{X_a R_\beta} \left\langle \omega_{R,\beta}^2 \right\rangle \right] u_{X,a} = -D\omega_{M,z}\omega_{R,a} \quad (6)$$

where the " $\langle \ldots \rangle$" symbol refers to spontaneous values. Note that the existence of $\left\langle \omega_{M,\beta}^2 \right\rangle$ and $\left\langle \omega_{R,\beta}^2 \right\rangle$ on the left-hand side of Eq. (6) implies that the resonant frequencies of the antipolar modes are naturally *quantitatively* affected by the condensation of oxygen octahedral tiltings because of the aforementioned biquadratic couplings.

Introducing now the time fluctuations of $\omega_{M,z}$ and $\omega_{R,a}$ on the right hand-side of Eq. (6) gives:

$$\sum_\beta \left[\left(2\pi\nu_a^X\right)^2 - (2\pi\nu)^2 - 2i\Gamma_a^X \pi\nu + B_{X_a M_\beta} \left\langle \omega_{M,\beta}^2 \right\rangle + B_{X_a R_\beta} \left\langle \omega_{R,\beta}^2 \right\rangle \right] u_{X,a} = - D\langle\omega_{M,z}\rangle\langle\omega_{R,a}\rangle - D\langle\omega_{R,a}\rangle\delta\omega_{M,z} - D\langle\omega_{M,z}\rangle\delta\omega_{R,a} \quad (7)$$

for $a = x$ or y, and where $\delta\omega_{M,z}$ and $\delta\omega_{R,a}$ represent the fluctuations of $\omega_{M,z}$ and $\omega_{R,a}$ with respect to their spontaneous $\langle\omega_{M,z}\rangle$ and $\langle\omega_{R,a}\rangle$ values.

Interestingly, averaging over time Eq. (7) will give on the left-hand side a quantity that is directly proportional to $\langle u_{X,a}\rangle$ and on the right-hand side a quantity that is simply $-D\langle\omega_{M,z}\rangle\langle\omega_{R,a}\rangle$ (since $\langle\delta\omega_{M,z}\rangle = \langle\delta\omega_{R,a}\rangle = 0$, by definition). As a result, the time-integration of Eq. (7) explains why, in our simulations depicted in Fig. 1, $\langle u_{X,a}\rangle$ becomes finite only after both $\langle\omega_{M,z}\rangle$ and $\langle\omega_{R,a}\rangle$ are nonzero. Note that if $\langle u_{X,a}\rangle$ condenses we are to take into account also the anharmonic contribution to the left part of Eq. (7).

Moreover, Eq. (7) also successfully explains why the oscillations of the x (respectively, y) component of $\boldsymbol{u}_X$ can couple with the fluctuations of the z-component of $\boldsymbol{\omega}_M$ and with the fluctuations of the x (respectively, y) component of $\boldsymbol{\omega}_R$ in the Pnma state, because of the existence of the last two terms on its right-hand side. Such dynamical mixing gives rise to the three peaks seen in each of Fig. 4a, f, g, and originates from the trilinear energy coupling since the D constant is involved in these last two terms. This mixing exists in Pnma but not in the cubic state because $\langle\omega_{R,x}\rangle$, $\langle\omega_{R,y}\rangle$ and $\langle\omega_{M,z}\rangle$ are finite in the former while vanishing in the latter state. In fact, the last two terms of Eq. (7) provide a deep insight into the mechanism of this mixing: the x-component (respectively, y-component) of $\boldsymbol{u}_X$ is able to dynamically couple with (i) the fluctuations of the z-component of $\boldsymbol{\omega}_M$ as soon as $\langle\omega_{R,x}\rangle$ (respectively, $\langle\omega_{R,y}\rangle$) is non-zero; and (ii) the oscillations of the x-component (respectively, y-component) of ω_R when $\langle\omega_{M,z}\rangle$ adopts a finite spontaneous value. These last two terms of Eq. (7) therefore also explain the mixing between antipolar and antiphase tilting modes in the P4/mbm state, for which only in-phase tiltings have condensed, i.e. even if there are no long-range ordered $\boldsymbol{u}_X$ and $\boldsymbol{\omega}_R$. In that case, item (ii) is valid, unlike item (i), which therefore explains why only two (and not three) peaks can be seen in Fig. 3a, g. In that situation, two modes, which where denoted as $\nu_{X_5^+,x,Pm\bar{3}m}$ and $\nu_{R_4^+,x,Pm\bar{3}m}$ in the cubic phase (that are pure antipolar and antiphase tilting modes, respectively), now interacts with each other in the P4/mbm phase to give rise to the mixed $\nu_{X_5^+,x,P4/mbm,LF}$ and $\nu_{X_5^+,x,P4/mbm,HF}$ modes.

Note that Eq. (7), as well as some of our numerical findings depicted in Figs. 2, 4 and 5, can also be used to predict the behavior of the phonon associated with the oscillations of $\boldsymbol{u}_X$ along the x (or y)-axis when the antiphase octahedral tiltings condense before the in-phase tilting in the structural path bringing the cubic state to Pnma (that is, if the phase transition sequence is Pm$\bar{3}$m, then Imma and finally Pnma when decreasing the temperature, which is another possible symmetry-allowed structural path to connect Pm$\bar{3}$m and Pnma, in addition to Pm$\bar{3}$m–P4/mbm–Pnma, according to ref. [36]). Equation (7) and our aforementioned numerical data then suggest that results will be very similar to those shown in Fig. 5a, that is (1) one hard $\nu_{X_5^+,x,Pm\bar{3}m}$ should exist in the cubic state; (2) there will be one soft phonon (to be denoted here as $\nu_{X_5^+,x,Imma,LF}$) and one hard phonon (to be coined $\nu_{X_5^+,x,Imma,HF}$) in the Imma state; and (3) one soft phonon at $\nu_{X_5^+,x,Pnma,LF}$ and two harder phonons at $\nu_{X_5^+,x,Pnma,MF}$ and $\nu_{X_5^+,x,Pnma,HF}$ in the Pnma state. The main anticipated difference between these predicted results and those shown in Fig. 5a is that $\nu_{X_5^+,x,Imma,LF}$ will arise from the mixing of the fluctuation of the x-component of $\boldsymbol{u}_X$ with the oscillation of the z-component of $\boldsymbol{\omega}_M$ that is mediated by the condensation of the x-component of $\boldsymbol{\omega}_R$, while $\nu_{X_5^+,x,P4/mbm,LF}$ of Fig. 5a involves the dynamical coupling between the x-component of $\boldsymbol{u}_X$ and the x-component of ω_R that is allowed when the z-component of ω_M has adopted a long-range-order. Interestingly, symmetry arguments[36] further indicate that the Pm$\bar{3}$m-to–Imma phase transition should be of first-order. As a result, we expect that the susceptibilities measured in the temperature interval for which these two phases can co-exist will have the features of both of these phases.

It is also worthwhile to realize that the present work and model most likely are not fully applicable to $PbZrO_3$ (which is often considered to be the prototype of antiferroelectrics), even if a trilinear energy coupling has been documented there as well.[37, 38] This is because it was recently proposed[39] that the unusual Pbam ground state of $PbZrO_3$ arises from an original *bilinear* coupling between antipolar motions and oxygen octahedral tiltings. As a result, Eqs. (4)–(7) should be generalized to further include such bilinear coupling too, when tackling dynamics of $PbZrO_3$ (note that refs. 40, 41 also suggested that flexoelectric effects can play some role in $PbZrO_3$ as well, which further emphasizes the need for a generalization of Eqs. (4)–(7) for that complex material).

In summary, we studied here $BiFeO_3$ bulk subject to hydrostatic pressure, as an example of perovskite materials having the paraelectric cubic $Pm\bar{3}m$ state at high temperature while adopting the antipolar Pnma phase at lower temperature. Our simulations first indicate that an intermediate state (of P4/mbm symmetry here) can exist for a narrow temperature range located in-between the temperature stability regions of $Pm\bar{3}m$ and Pnma—as also consistent with symmetry analyses.[36] We also reveal that antipolar modes have rather high resonant frequencies that are nearly independent of the temperature within $Pm\bar{3}m$, while they can become very soft in the intermediate state and in the Pnma phase because of very specific *dynamical* mixings with (the soft) oxygen octahedral tiltings. Such mixings increase the number of phonon modes possessing antipolar character when passing through the $Pm\bar{3}m$–P4/mbm and P4/mbm–Pnma transitions. Moreover, a simple model is developed allowing to not only explain all these features but also to reveal that they arise from a trilinear energy coupling antipolar motions, in-phase and anti-phase tiltings. This model can also be used to predict dynamics of antipolar modes in case of the $Pm\bar{3}m$–Imma-Pnma transition. We hope that the present study is of large importance for the scientific community, especially when realizing that (i) Pnma is the most abundant ground state of perovskites[23, 24]; and (ii) trilinear energetic couplings can also give rise to the formation of electrical polarization in the so-called hybrid improper ferroelectrics,[1–7] implying that our present study is a good starting point to tackle and understand polarization dynamics in these particular systems that are intensively currently investigated too.

METHODS

Here, the effective Hamiltonian approach of refs. 28, 42–44 is used in order to investigate properties of $BiFeO_3$ (BFO) at finite temperatures and under hydrostatic pressure. The degrees of freedoms of this Hamiltonian are (i) the local soft mode $\boldsymbol{u}_i$ centered on the Bi sites (such centering allows, e.g., to reproduce the Bi-driven antipolar motions associated with the Pnma phase of BFO[28]); (ii) the η– homogenous strain tensor; (iii) the pseudo-vector $\boldsymbol{\omega}_i$, which is centered on Fe ions and characterizes oxygen octahedral tiltings[34] (also known as antiferrodistortive (AFD) distortions) in unit cell i. For instance, $\boldsymbol{\omega}_i = 0.1\ \mathbf{z}$, where $\mathbf{z}$ is the unit vector along the z-axis, indicates that the oxygen octahedron centered around the Fe site i tilts about 0.1 radians about the z-axis; (iv) the magnetic dipole moment m_i, which is Fe-centered too and whose magnitude is equal to $4\mu_B$, as consistent with first principles[45] and measurements[46]; and (v) the inhomogeneous strain characterized by dimensionless variable $\boldsymbol{v}_i$.[47, 48] The total effective Hamiltonian is the sum of the following three main terms

$$E_{total} = E_1(\{u_i\},\{\eta\},\{v_i\}) + E_2(\{m_i\},\{u_i\},\{\eta\},\{v_i\},\{\omega_i\}) + E_3(\{u_i\},\{\eta\},\{v_i\},\{\omega_i\}), \quad (8)$$

where E_1 represents the energy associated with the local modes, elastic strain interactions, and coupling between the local modes and strain; E_2 ensembles the energies correlated with the magnetic degrees of freedom and their couplings with the local modes, strains and AFD distortions; and E_3 describes the energetics involving the AFD interactions and their couplings with the local modes and strains. Analytical expressions for E_1 and E_2 are provided in refs. 47, 48 and ref. 42, respectively. The expression for E_3 has been described in ref. 28 and is as follows:

$$\begin{aligned} E_3(\{u_i\},\{\eta\},\{v_i\},\{\omega_i\}) &= \sum_i \left[\kappa_A\omega_i^2 + \alpha_A\omega_i^4 + \gamma_A\left(\omega_{ix}^2\omega_{iy}^2 + \omega_{iy}^2\omega_{iz}^2 + \omega_{ix}^2\omega_{iz}^2\right)\right] \\ &+ \sum_{ij}\sum_{\alpha\beta} K_{ij\alpha\beta}\omega_{i\alpha}\omega_{j\beta} + \sum_i\sum_\alpha K'\omega_{i,\alpha}^3\left(\omega_{i+\alpha,\alpha} + \omega_{i-\alpha,\alpha}\right) \\ &+ \sum_i\sum_{\alpha\beta} C_{l\alpha\beta}\eta_l(i)\omega_{i\alpha}\omega_{i\beta} \\ &+ \sum_{i,j}\sum_{\alpha,\beta} D_{ij,\alpha\beta}u_{j,\alpha}\omega_{i,\alpha}\omega_{i,\beta} + \sum_{i,j}\sum_{\alpha\beta\gamma\delta} E_{\alpha\beta\gamma\delta}\omega_{i\alpha}\omega_{j\beta}u_{j\gamma}u_{i\delta} \end{aligned} \quad (9)$$

where the sum over i runs over all Fe-sites, and where α and β are Cartesian components along the x–, y–, and z-axes coinciding with the pseudocubic [100], [010], and [001] directions respectively. Moreover, $\eta_l(i)$ is the l-th component of the total strain (in Voigt notation), including the homogeneous and inhomogeneous strain, at site i. The first three energies of Eq. (9) were proposed and/or used in refs. 28, 42–44 and characterize onsite interactions of the AFD distortions. The fourth and fifth energies represent AFD short-range interactions and were provided in ref. 43 and ref. 28, respectively. Note that, in this fifth energy, $\omega_{i+\alpha,\alpha}$ is the α-component of the AFD mode at the site shifted from the Fe site i to its nearest Fe neighbor along the axis α. The sixth energy describes the coupling between oxygen octahedral tiltings and strains. The seventh energy was introduced in ref. 28, and represents an anharmonic (trilinear) interaction energy between the local mode u centered on a Bi site and two AFD distortions centered on Fe sites. Finally, the eighth energy of Eq. (9) characterizes bi-quadratic interactions between oxygen octahedral tiltings and local modes, as given in ref. 43. More details about E_1 and E_3, including the values of parameters, are provided in the Supplementary Materials.

We employ such effective Hamiltonian to conduct Monte-Carlo simulations of BFO under pressure. Note that we simulate the effects of applying a pressure by adding an energy that involves the products between the hydrostatic pressure and strain tensor elements. We then perform MD calculations by using 4×10^5 MD steps with a time step of 0.5 fs as similar to what was done in ref. 49, except that the effective Hamiltonian used here has local modes that are centered on Bi ions (and not on Fe ions like in ref. 49). As a result, the fifth and seventh terms of Eq. (9) are presently incorporated into the dynamics of BFO.

Data availability

All data are provided in full in the Results section of this paper.

ACKNOWLEDGEMENTS

K.P thanks ARO Grant No.W911NF-16-1-0227, while S.P. and L.B. acknowledge the support of Air Force Office of Scientific Research under Grant No. FA9550-16-1-0065 S.P appreciates also the grants 3.1649.2017/4.6 from RMES (Russian Ministry of Education and Science) and 16-52-0072_Bel_a from RFBR (Russian Foundation for Basic Research).

AUTHOR CONTRIBUTIONS

K.P carried out the atomistic calculations reported here. S.P. developed the theoretical model that is related to Eqs. (4)–(7). All authors contributed to the interpretation of the results and to the writing of the paper.

ADDITIONAL INFORMATION

Supplementary Information accompanies the paper on the *npj Computational Materials* website (doi:10.1038/s41524-017-0033-z).

Competing Interests: The authors declare no competing financial interests.

Publisher's note: Springer Nature remains neutral with regard to jurisdictional claims in published maps and institutional affiliations.

REFERENCES

1. Benedek, N. A. & Fennie, C. J. Hybrid improper ferroelectricity: A mechanism for controllable polarization-magnetization coupling. *Phys. Rev. Lett.* **106**, 107204 (2011).
2. Rondinelli, J. M. & Fennie, C. J. Ferroelectricity: Octahedral rotation-induced ferroelectricity in cation ordered perovskites. *Adv. Mater.* **24**, 1961–1968 (2012).

3. Xu, B. et al. Hybrid improper ferroelectricity in multiferroic superlattices: Finite-temperature properties and electric-field-driven switching of polarization and magnetization. *Adv. Funct. Mater.* **25**, 3626–3633 (2015).
4. Mulder, A. T., Benedek, N. A., Rondinelli, J. M. & Fennie, C. J. Turning ABO_3 antiferroelectrics into ferroelectrics. *Adv. Funct. Mater.* **23**, 4810–4820 (2013).
5. Zanolli, Z., Wojdel, J. C., Íñiguez, J. & Ghosez, P. Electric control of the magnetization in $BiFeO_3/LaFeO_3$ superlattices. *Phys. Rev. B* **88**, 060102 (2013). (R).
6. Bousquet, E. et al. Improper ferroelectricity in perovskite oxide artificial superlattices. *Nature.* **452**, 732–736 (2008).
7. Zhao, H. J., Íñiguez, J., Ren, W., Chen, X. M. & Bellaiche, L. Atomistic theory of hybrid improper ferroelectricity in perovskites. *Phys. Rev. B* **89**, 174101 (2014).
8. Yang, Y., Íñiguez, J., Mao, A. J. & Bellaiche, L. Prediction of a novel magnetoelectric switching mechanism in multiferroics. *Phys. Rev. Lett.* **112**, 057202 (2014).
9. Varignon, J., Bristowe, N. C. & Ghosez, P. Electric field control of Jahn-Teller distortions in bulk perovskites. *Phys. Rev. Lett.* **116**, 057602 (2016).
10. Varignon, J., Bristowe, N. C., Bousquet, E. & Ghosez, P. Coupling and electrical control of structural, orbital and magnetic orders in perovskites. *Sci. Rep* **5**, 15364 (2015).
11. Xu, C. *et al*. Pressure-induced multiferroics via Pseudo Jahn-Teller effects and novel couplings. *Adv. Func. Mater*. **27**, 1604513 (2017).
12. Bellaiche, L. & Íñiguez, J. Universal collaborative couplings between oxygen-octahedral rotations and antiferroelectric distortions in perovskites. *Phys. Rev. B* **88**, 014104 (2013).
13. Xu, B., Paillard, C., Dkhil, B. & Bellaiche, L. Pinched hysteresis loop in defect-free ferroelectric materials. *Phys. Rev. B* **94**, 140101 (2016). (R).
14. Xu, B., Íñiguez, J. & Bellaiche, L. Designing lead-free antiferroelectrics for energy storage. *Nat. Comm* **8**, 15682 (2017).
15. Rabe, K. M. Antiferroelectricity in Oxides: A Reexamination, in *Functional Metal Oxides: New Science and Novel Applications* (eds Ogale, S. B., Venkatesan, T. V. & Blamire, M. G.) (Wiley-VCH Verlag GmbH & Co. KGaA, 2013).
16. Ma, B., Kwon, D. K., Narayanan, M. & (Balu) Balachandran, U. Dielectric properties and energy storage capability of antiferroelectric $Pb_{0.92}La_{0.08}Zr_{0.95}Ti_{0.05}O_3$ film-on-foil capacitors. *J. Mater. Res.* **24**, 2993–2996 (2009).
17. Ma, B., Narayanan, M. & Balachandran, U. Dielectric strength and reliability of ferroelectric PLZT films deposited on nickel substrates. *Mater. Lett.* **63**, 1353–1356 (2009). (Balu).
18. Hao, X., Wang, Y., Zhang, L., Zhang, L. & An, S. Composition-dependent dielectric and energy-storage properties of $(Pb,La)(Zr,Sn,Ti)O_3$ antiferroelectric thick films. *Appl. Phys. Lett.* **102**, 163903 (2013).
19. Chu, B. et al. A dielectric polymer with high electric energy density and fast discharge speed. *Sci* **313**, 334–336 (2006).
20. Correia, T. M., McMillen, M., Rokosz, M. & Cain, M. G. A lead-free and high-energy density ceramic for energy storage applications. *J. Am. Ceram. Soc.* **96**, 2699–2702 (2013).
21. Peng, B. et al. Giant electric energy density in epitaxial lead-free thin films with coexistence of ferroelectrics and antiferroelectrics. *Adv. Electron. Mater* **1**, 1500052 (2015).
22. Park, M. H. et al. Thin $Hf_xZr_{1-x}O_2$ films: A new lead-free system for electrostatic supercapacitors with large energy storage density and robust thermal stability. *Adv. Energy Mater* **4**, 1400610 (2014).
23. Benedek, N. A. & Fennie, C. J. Why are there so few perovskite ferroelectrics? *Phys. Chem. C* **117**, 13339–13349 (2013).
24. Lufaso, M. W. & Woodward, P. M. Prediction of the crystal structures of perovskites using the software program SPuDS. *Acta. Cryst* **B57**, 725–738 (2001).
25. Buhot, J. et al. Driving Spin Excitations by Hydrostatic Pressure in $BiFeO_3$. *Phys. Rev. Lett.* **115**, 267204 (2015).
26. Guennou, M. et al. Multiple high-pressure phase transitions in $BiFeO_3$. *Phys. Rev. B* **84**, 174107 (2011).
27. Gomez-Salces, S. et al. Effect of pressure on the band gap of the local FeO_6 environment in $BiFeO_3$. *Phys. Rev. B* **85**, 144109 (2012).
28. Prosandeev, S., Wang, D., Ren, W., Íñiguez, J. & Bellaiche, L. Novel nanoscale twinned phases in perovskite oxides. *Adv. Funct. Mater.* **23**, 234–240 (2013).
29. Arnold, D. C., Knight, K. S., Morrison, F. D. & Lightfoot, P. Ferroelectric-paraelectric transition in $BiFeO_3$: Crystal structure of the orthorhombic β phase. *Phys. Rev. Lett.* **102**, 027602 (2009).
30. Wang, H. et al. Stabilization of highly polar $BiFeO_3$-like structure: A New interface design route for enhanced ferroelectricity in artificial perovskite superlattices. *Phys. Rev. X* **6**, 011027 (2016).
31. Weerasinghe, J., Wang, D. & Bellaiche, L. Low-frequency coupled modes in disordered $Pb(Zr,Ti)O_3$ solid solutions from first principles. *Phys. Rev. B* **85**, 014301 (2012).
32. Wang, D. et al. Fano resonance and dipolar relaxation in lead-free relaxors. *Nature communication* **5**, 5100 (2014).
33. Ponomareva, I., Bellaiche, L., Ostapchuk, T., Hlinka, J. & Petzelt, J. Terahertz dielectric response of cubic $BaTiO_3$. *Phys. Rev. B* **77**, 012102 (2008).
34. Kornev, I. A., Bellaiche, L., Janolin, P. E., Dkhil, B. & Suard, E. Phase diagram of $Pb(Zr,Ti)O_3$ solid solutions from first principles. *Phys. Rev. Lett.* **97**, 157601 (2006).
35. Al-Zein, A., Hlinka, J., Rouquette, J. & Hehlen, B. Soft mode doublet in $PbMg_{1/3}Nb_{2/3}O_3$ relaxor investigated with Hyper-Raman scattering. *Phys. Rev. Lett.* **105**, 017601 (2010).
36. Howard, C. J. & Stokes, H. T. Group-theoretical analysis of octahedral tilting in perovskites. *Acta Cryst* **B54**, 782–789 (1998).
37. Hlinka, J. et al. Multiple soft-mode vibrations of lead zirconate. *Phys. Rev. Lett.* **112**, 197601 (2014).
38. Íñiguez, J., Stengel, M., Prosandeev, S. & Bellaiche, L. First-principles study of the multimode antiferroelectric transition in $PbZrO_3$. *Phys. Rev. B* **90**, 220103 (2014). (R).
39. Patel, K. et al. Atomistic mechanism leading to complex antiferroelectric and incommensurate perovskites. *Phys. Rev. B* **94**, 054107 (2016).
40. Burkovsky, R. G. et al. Lattice dynamics and antiferroelectricity in $PbZrO_3$ tested by x-ray and Brillouin light scattering. *Phys. Rev. B* **90**, 144301 (2014).
41. Tagantsev, A. K. et al. The origin of antiferroelectricity in $PbZrO_3$. *Nat. Comm* **4**, 2229 (2013).
42. Albrecht, D. et al. Ferromagnetism in multiferroic $BiFeO_3$ films: A first-principles-based study. *Phys. Rev. B.* **81**, 140401 (2010). (R).
43. Kornev, I. A., Lisenkov, S., Haumont, R., Dkhil, B. & Bellaiche, L. Finite-temperature properties of multiferroic $BiFeO_3$. *Phys. Rev. Lett.* **99**, 227602 (2007).
44. Lisenkov, S., Kornev, I. A. & Bellaiche, L. Erratum: Properties of multiferroic $BiFeO_3$ under high magnetic fields from first principles. *Phys. Rev. B* **79**, 012101 (2009).
45. Neaton, J. B., Ederer, C., Waghmare, U. V., Spaldin, N. A. & Rabe, K. M. First-principles study of spontaneous polarization in multiferroic $BiFeO_3$. *Phys. Rev. B* **71**, 014113 (2005).
46. Fischer, P., Polomska, M., Sosnowska, I. & Szymanski, M. Temperature dependence of the crystal and magnetic structures of $BiFeO_3$. *J. Phys. C: Solid St. Phys* **13**, 1931–1940 (1980).
47. Zhong, W., Vanderbilt, D. & Rabe, K. M. Phase transitions in $BaTiO_3$ from first principles. *Phys. Rev. Lett.* **73**, 1861 (1994).
48. Zhong, W., Vanderbilt, D. & Rabe, K. M. First-principles theory of ferroelectric phase transitions for perovskites: The case of $BaTiO_3$. *Phys. Rev. B* **52**, 6301 (1995).
49. Wang, D., Weerasinghe, J. & Bellaiche, L. Atomistic Molecular Dynamic Simulations of Multiferroics. *Phys. Rev. Lett.* **109**, 067203 (2012).